Earth and Planetary Science Letters 574 (2021) 117172

Contents lists available at ScienceDirect

Earth and Planetary Science Letters

www.elsevier.com/locate/epsl

Carbonate associated sulfate (CAS) $\delta^{34}S$ heterogeneity across the End-Permian Mass Extinction in South China

Daniel L. Johnson [a,*,1], Theodore M. Present [a], Menghan Li [b], Yanan Shen [b], Jess F. Adkins [a]

[a] Division of Geological & Planetary Sciences, California Institute of Technology, 1200 E. California Blvd., Pasadena, CA 91125, USA
[b] School of Earth and Space Sciences, University of Science and Technology of China, Hefei, 230026, China

ARTICLE INFO

Article history:
Received 1 April 2021
Received in revised form 30 July 2021
Accepted 13 August 2021
Available online xxxx
Editor: L. Derry

Keywords:
End Permian Mass Extinction
Permo-Triassic Extinction
sulfur cycle, sulfur isotopes
carbonate associated sulfate

ABSTRACT

The dynamics of the marine sulfur cycle across the End-Permian Mass Extinction (EPME) have been obscured by disagreement between sulfur isotopic records from different archives. Here, we attempt to resolve this disagreement with new measurements of carbonate associated sulfate (CAS) $\delta^{34}S$ (i.e., $\delta^{34}S_{CAS}$) from three Permian-Triassic boundary (PTB) sections in South China. We observe substantial $\delta^{34}S_{CAS}$ variation within single hand samples, with most samples having a $\delta^{34}S_{CAS}$ range exceeding 5‰ and some reaching ~20‰. We also find evidence for mixing between low CAS abundance, high $\delta^{34}S_{CAS}$ and high CAS abundance, low $\delta^{34}S_{CAS}$ phases. A simple model of reduced sulfur oxidation and incorporation as CAS suggests that sedimentary redox oscillations may plausibly explain the $\delta^{34}S_{CAS}$ heterogeneity within many EPME carbonates; rapid variation in the $\delta^{34}S$ of the marine SO_4^{2-} reservoir is not necessary. Additional work to examine how synchronous changes in organic carbon fluxes, sedimentation rates, or other parameters that impact sediment redox and sulfur diagenesis is needed to evaluate the environmental implications of the $\delta^{34}S_{CAS}$ heterogeneity.

1. Introduction

The End-Permian Mass Extinction (EPME) is the largest known mass extinction event in Earth's history (Sepkoski, 1981; Erwin, 2006). Paleobiological datasets suggest that nearly 80% of genera went extinct, with losses especially concentrated in calcified marine invertebrates (Payne and Clapham, 2012). Geochronological studies have shown that this extinction was rapid, with zircon U-Pb age measurements constraining the duration of the extinction in South China to 60 ± 48 kyr (Burgess et al., 2014). Catastrophic extinction mechanisms have been proposed based on this rapidity, with prior work (e.g. Knoll et al., 2007) suggesting a massive influx of carbon to the ocean-atmosphere system as a primary causal factor.

Past geochemical studies have revealed large marine chemistry perturbations associated with the EPME. Observations of laminated, pyrite-rich sediments in Permian-Triassic boundary (PTB) strata suggested widespread ocean anoxia and euxinia during the extinction interval (e.g. Bond and Wignall, 2010). Carbon isotope studies (e.g. Payne et al., 2004) identified a gradual late Permian carbonate $\delta^{13}C$ decline punctuated by a rapid, large (3-4‰) negative excursion across the extinction event. Similarly dramatic changes occurred in the strontium (e.g. Korte et al., 2004), calcium (e.g. Hinojosa et al., 2012), osmium (e.g. Schoepfer et al., 2013), uranium (e.g. Lau et al., 2016), and nitrogen (e.g. Schoepfer et al., 2013) isotope systems. The Siberian Traps have emerged as the most likely source of the disturbance that caused the EPME, with volatilization of sedimentary organic carbon (Svensen et al., 2009) possibly augmenting the eruption's CO_2 release and its ^{13}C depletion.

Numerous studies (e.g. Kaiho et al., 2001; Luo et al., 2010; Song et al., 2014) have measured the sulfur (S) isotopic composition of carbonate associated sulfate (CAS) to study the global marine S cycle across the EPME. These studies have documented a huge range in CAS $\delta^{34}S$ (i.e., $\delta^{34}S_{CAS}$), leading some authors (e.g. Luo et al., 2010) to argue for very low (< 5 mM) seawater sulfate (SO_4^{2-}) concentrations at the time of the EPME. Other studies (e.g. Newton et al., 2004) have alternatively suggested mixing of isotopically disparate reservoirs of S. Although both CAS and evaporite $\delta^{34}S$ records (e.g. Bernasconi et al., 2017) indicate a large increase in seawater $\delta^{34}S$ across the PTB, disagreement between records has inhibited a better understanding of marine S cycle behavior.

Relatively low CAS abundances (e.g. Marenco et al., 2008) make end-Permian carbonates a prime target for $\delta^{34}S$ studies utilizing methods with minimal sample requirements. Here, we present

* Corresponding author.
E-mail address: Dan.Johnson@rice.edu (D.L. Johnson).
[1] Current address: Department of Earth, Environmental & Planetary Sciences, Rice University, 6100 Main St., Houston, TX 77005, USA.

https://doi.org/10.1016/j.epsl.2021.117172
0012-821X/

Fig. 1. End-Permian paleogeographic map. Red stars denote the approximate locations of the three sections included in this study. Small yellow stars denote locations of other EPME sections with $\delta^{34}S_{CAS}$ data. Map after Scotese (2014). (For interpretation of the colors in the figure(s), the reader is referred to the web version of this article.)

new multicollector inductively coupled plasma mass spectrometry (MC-ICP-MS) $\delta^{34}S_{CAS}$ data from three EPME sections in South China. We find that $\delta^{34}S_{CAS}$ heterogeneity within single hand samples often exceeds 5‰ and sometimes reaches ~20‰. Cross plots of $\delta^{34}S_{CAS}$ versus the inverse of CAS abundance suggest this heterogeneity results from mixing between phases. We argue that the disagreement between evaporite and CAS $\delta^{34}S$ records likely indicates incorporation of SO_4^{2-} derived from reduced S oxidation into CAS; i.e., the $\delta^{34}S_{CAS}$ variability reflects diagenetic alteration, not primary variation in the $\delta^{34}S$ of marine SO_4^{2-}.

2. Sample localities

An End-Permian paleogeographic map depicting the sample localities for this study and selected localities from previous studies is shown in Fig. 1. Meishan (31.0798°N, 119.7058°E) is the location of the Global Boundary Stratotype Section and Point (GSSP) for the Permian-Triassic boundary (Hongfu et al., 2001) and has been extensively targeted for geochemical studies (e.g. Kaiho et al., 2001; Cao et al., 2002, 2009; Riccardi et al., 2006; Burgess et al., 2014). Here, carbonate sediments were deposited in a carbonate ramp setting within a local topographic depression between fair weather and storm wave base (Hongfu et al., 2001; Chen et al., 2015). Facies include bioclastic micrite, wackestones, packstones, and grainstones containing abundant pyrite and fossils of brachiopods, crinoids, conodonts, foraminifera, and other calcified organisms (Hongfu et al., 2001; Zheng et al., 2013; Chen et al., 2015). The section is highly condensed and includes multiple ash beds that have been precisely dated through U-Pb zircon geochronology (e.g. Burgess et al., 2014); estimated sedimentation rates based on current age constraints range from < 0.1 m/Myr to 0.68 m/Myr (Burgess et al., 2014). Data presented in this study come from beds 24 through 29 (Hongfu et al., 2001), an interval in which the estimated sedimentation rates do not exceed 26 m/Myr.

Yudongzi (32.0765°N, 105.1546°E) is situated to the west of Meishan in the Sichuan Basin. Here, sediments were deposited on the continental shelf, likely near the margin of a rimmed carbonate platform (Tang et al., 2017). The section is relatively unstudied, although recent work (Kershaw et al., 2012; Tang et al., 2017; Zhang et al., 2020b) has begun to characterize the biostratigraphy and lithofacies of the site. The stratigraphy includes boundstones and skeletal grainstones within the latest Permian Changxing Formation and thrombolitic microbialites, lime mudstones, and grainstones in the earliest Triassic Feixianguan Formation (Kershaw et al., 2012; Tang et al., 2017; Zhang et al., 2020b). The exact position of the Permian-Triassic boundary at the site is uncertain; the first appearance datum (FAD) of the conodont *H. parvus* is 0.5 m above the base of the Feixianguan Formation, but the boundary may be at the Changxing-Feixianguan contact. A prominent erosional disconformity is evident at the contact between the Changxing and Feixianguan formations, with an unknown amount of material missing (Tang et al., 2017). Absolute ages at the site are not well constrained, but the occurrence of a thick (~11 m) section of microbialite suggests that the section is highly expanded (Tang et al., 2017). Correlation of the extinction interval at the site with that at Meishan (Burgess et al., 2014) indicates that absolute sedimentation rates at Yudongzi are at least an order of magnitude higher (> 100 m Myr) than the lowest sedimentation rates at Meishan.

Penglaitan (23.6946°N, 109.3110°E) is located along the Hongshui River to the south of Yudongzi and Meishan in the Nanpanjiang Basin. This section serves as the GSSP for the Capitanian-Wuchiapingian boundary and was deposited near the eastern carbonate platform within the basin (Jin et al., 2006; Shen et al., 2019). The stratigraphy near the Permo-Triassic boundary consists primarily of peritidal mudstones, wackestones, and packstones deposited in a peritidal carbonate ramp setting (Shen et al., 2007, 2019). The Permo-Triassic boundary is located at the boundary between Beds 141 and 142 in the section, which marks the transition from limestones and tuffs in the uppermost Talung Formation to mixed black shales and limestones in the Early Triassic Loulou Formation (Shen et al., 2007, 2019). Volcaniclastic sediments are extremely abundant near the boundary. Zircon U-Pb ages from these sediments suggest a very high sedimentation rate of 69 cm/kyr

(690 m/Myr) for the uppermost part of the Talung Formation (Shen et al., 2019).

3. Methods

Hand samples were collected in the field prior to this study. To enable visual sample assessment, hand samples were cut using a rock saw to expose fresh surfaces and polished on a Covington vibratory lathe using 240-grit silicon carbide, 600-grit aluminum oxide, and 9.5 micron aluminum oxide in sequence. Polished surfaces were imaged under an optical microscope and examined for grain size, pyrite abundance, and biogenic contents. Following optical imaging, a representative subset of twelve samples was selected for μ-XRF microscopy characterization and imaged using a Bruker M4 Tornado μ-XRF spectrometer. Images were typically collected under vacuum with a 240 µA, 50 keV X-ray beam using a 10 ms dwell time and 20 µm spot size. After imaging, XRF data were exported and loaded into MATLAB® for a principal component analysis (PCA) to identify distinct phases. Counts data for all elements (Al, Ba, Ca, Fe, K, Mg, Mn, Na, P, Rh, S, Si, Sr, and Ti) at each pixel were imported into a single matrix and subjected to PCA using MATLAB®'s built-in `pca` function. Maps of the first three principal components were visually inspected and used to identify regions for targeted sampling.

Samples were drilled with dental burs using a Dremel tool. Areas were targeted for sampling such that each of the main principal components evident from the PCA analysis was sampled at least once. Either two or three distinct areas were drilled from each hand sample. Collected powders (3 to 15 mg in mass) were subsequently cleaned and subjected to column chemistry to isolate CAS. Powders were submerged in 1 mL 10% (w/w) NaCl solution under sonication for at least four hours to remove soluble sulfate unassociated with the carbonate crystal lattice and were subsequently rinsed five times with 18.2 MΩ Millipore Milli-Q water. Samples were then dried down, weighed, dissolved in 0.5 N Seastar® HCl, dried down again, and taken up in 0.5% (v/v) Seastar® HCl for column chemistry. Sulfate from each sample was isolated on an anion exchange column containing 0.8 mL of Bio-Rad® AG1-X8 resin preconditioned with 2 x 10 column volumes of 10% (v/v) reagent grade HNO3, 2 x 10 column volumes of 33% (v/v) reagent grade HCl, and 2 x 10 column volumes of 0.5% Seastar® HCl. Quality control was maintained by including at least one seawater, one deep sea coral, and one procedural blank within each set of columns. After column chemistry, samples were dried down, re-diluted, and an aliquot measured for SO_4^{2-} concentration using a Dionex ICS-3000 ion chromatography system equipped with a 2 mm AS4A-SC column and 1.8 mM Na_2CO_3/1.7 mM $NaHCO_3$ eluent.

S isotope ratios were measured on a Thermo-Fischer Neptune Plus MC-ICP-MS following the methods of Paris et al. (2013). SO_4^{2-} concentration measurements were used to ensure that sample concentrations matched the bracketing standard concentration (10 µM Na_2SO_4) as closely as possible. Average procedural blank (n = 6) size and $\delta^{34}S$ were 0.39 ± 0.21 nanomoles and 4.3 ± 3.2‰, respectively. The average seawater $\delta^{34}S$ (n = 4) was 21.05 ± 0.02‰, and the average deep sea coral $\delta^{34}S_{CAS}$ (n = 3) was 22.7 ± 0.5‰.

4. Results

4.1. μ-XRF maps

Example μ-XRF elemental maps and PCA maps are depicted in Supplementary Figures 1 and 2, respectively (Supplementary Material). Although the elemental maps display some variability in elemental count intensities, the PCA maps are more effective in assigning this variation to different components. The first principal component in the example depicted in Supplementary Figure 2 (sample YDS 32.5) shows a strong positive association with Ca, and the second component a strong association with Fe and S. These two components are ubiquitous throughout all samples. Cross plots of elemental counts also commonly demonstrate positive correlations between Fe and S and between Al and Si (Supplementary Figure 3). Other elemental cross plots either show no correlation or have too few counts of at least one element for the correlation to be robust.

4.2. $\delta^{34}S_{CAS}$ measurements

Our $\delta^{34}S_{CAS}$ data are listed in table form in Table 1 and are plotted against stratigraphic height in Supplementary Figures 4-6 (Supplementary Material). In Fig. 2, we plot $\delta^{34}S_{CAS}$ against the inverse of CAS abundance. CAS abundance ([CAS]) and $\delta^{34}S_{CAS}$ values vary widely within single hand samples. Across all samples, [CAS] ranges from a minimum of 32 ± 3 ppm to a maximum of 1787 ± 195 ppm. [CAS] within hand samples sometimes differs by a factor of two or more. $\delta^{34}S_{CAS}$ values are similarly variable; the average range of $\delta^{34}S_{CAS}$ within single hand samples is 7.8‰, and the median range is 5.9‰. Seven samples feature $\delta^{34}S_{CAS}$ heterogeneity that exceeds 10‰, with three reaching ~20‰. Such variation is unassociated with changes in the stratigraphy or the carbonate $\delta^{13}C$ profiles at each site (Supplementary Material).

5. Discussion

5.1. μ-XRF mapping as a screening tool

Most prior studies of the geochemistry of carbonates have used diagenetic screening methods that are qualitative (e.g. optical microscopy) or are limited to discrete points within samples (e.g. ICP-MS elemental abundance measurements) (Grossman et al., 1991, 1993; Veizer et al., 1999). Although such methods are important for interpreting isotopic variation within samples, they are often laborious and may provide little context about chemical variation within the sample beyond the area selected for measurement. The results presented here show μ-XRF microscopy to be a powerful tool that can provide information similar to that offered by traditional methods in a less laborious, more spatially extensive, and nondestructive manner. Principal component analysis on elemental counts data effectively identifies different dominant phases within cut and polished hand samples. The method is especially effective for identifying pyrite that may be difficult to observe under optical microscopy (e.g. Supplementary Figure 3B); this is important for minimizing the risk of contamination of CAS measurements by sulfur derived from reduced phases. While we did not attempt to make quantitative abundance estimates here, there is significant potential to use μ-XRF microscopy as a substitute for more traditional chemical methods of quantifying elemental abundances. Careful calibration with standards and longer dwell times would be required to quantify abundances for trace components of carbonates; still, the non-destructive nature of μ-XRF microscopy makes it particularly advantageous for screening samples for diagenetic alteration. Future work should test the accuracy and precision of abundance quantification with this method and compare analytical times to the time required for traditional chemical measurements to evaluate whether replacement of chemical (e.g. ICP-OES) measurements with μ-XRF measurements may be possible.

5.2. Within-sample $\delta^{34}S_{CAS}$ heterogeneity

Previous studies (e.g. Present et al., 2015, 2019) have found large $\delta^{34}S_{CAS}$ variations among different phases within bulk carbonate hand samples. Our measurements support these findings.

Table 1
$\delta^{34}S_{CAS}$ data.

Locality	Sample ID	Height (m)	Description	[CAS] #1 (ppm)	2σ	[CAS] #2 (ppm)	2σ	[CAS] #3 (ppm)	2σ	CAS δ^{34}S #1 (‰)	2σ	CAS δ^{34}S #2 (‰)	2σ	CAS δ^{34}S #3 (‰)	2σ
Meishan	29-1	4.42	grayish-green calcareous mudstone, few to no bioclasts	1551	189	837	94	1100	143	−5.4	0.2	13.9	0.4	8.4	0.6
Meishan	24-A-down	3.2	dark grey bioclastic wackestone	819	88	1787	195			3.7	0.2	−10.1	0.2		
Meishan	23-5	2.665	dark grey bioclastic mudstone	795	82	1130	117			22.2	0.2	21.4	0.2		
Meishan	23-2-up	2.285	dark grey bioclastic mudstone	928	95	869	89			22.6	0.2	22.2	0.2		
Meishan	23-1-up-B	1.963	dark grey bioclastic mudstone	620	64	761	78	458	48	29.7	0.2	16.6	0.3	26.7	0.3
Yudongzi	YDS 34.5	34.5	wackestone with few identifiable biogenic clasts and sparry matrix	65	7	88	9	62	6	20.7	0.5	19.5	0.5	20.1	0.4
Yudongzi	YDS 32.5	32.5	wackestone with calcite spar, veins rich in pyrite and siliclastic material, and disseminated pyrite	345	37	292	30	301	31	21.3	0.5	22.0	0.3	19.8	0.3
Yudongzi	YDS 31.5	31.5	microbialitic packstone with many well-preserved biogenic grains, including brachiopod fragments and forams; weathered and recrystallized near top of sample with many sparry/recrystallized veins	242	25	545	55	211	22	17.2	0.4	−1.4	0.2	15.7	0.7
Yudongzi	YDS 21	21	microbialitic wackestone w/some brachiopod fragments, thin veins of spar and pyrite	748	77	741	78			12.5	0.2	10.2	0.5		
Yudongzi	YDS 13	13	wackestone w/many mm-width veins of spar/recrystallized carbonate	46	5	95	10			27.5	1.0	21.7	0.6		
Yudongzi	YDS 1.5	1.5	mudstone w/o obvious biogenic grains; zones of spar, dissolution, and abundant pyrite	57	6	42	4	32	3	21.2	–	20.6	0.7	22.2	1.0
Yudongzi	YDS 0	0	mudstone w/o obvious biogenic grains; zones of spar, dissolution, and abundant pyrite	65	7	64	7			15.7	–	19.4	0.5		
Penglaitan	PLT-09 67	67	silty, laminated carbonate mudstone	256	31	239	27	520	89	2.8	2.1	3.0	2.5		
Penglaitan	PLT-09 63.7	63.7	bioclastic packstone with calcite veins	668	49	638	46	710	52	9.4	0.5	6.1	0.6	3.2	0.5
Penglaitan	PLT-09 63.3	63.3	wavy-laminated gray packstone with mouldic calcite cement	654	47	838	62	587	43	5.6	0.4	−6.3	0.7	4.4	0.5
Penglaitan	PLT-09 62.7	62.7	bioclastic packstone with calcite veins	354	27	279	21	155	7	9.8	0.8	3.4	1.6	−6.0	3.3
Penglaitan	PLT-09 62.7 foram	62.7	foram-rich area within packstone	219	28					6.2	2.7				
Penglaitan	PLTN-12-G 61.85	61.85	veined, gray foram-bearing packstone	209	15	294	21			−13.3	2.1	−14.2	0.8		
Penglaitan	PLTN-12-G 61.85 vein	61.85	veins within packstone	148	10	242	17			6.0	1.7	4.1	0.7		
Penglaitan	PLTN-12-G 48.1	48.1	gray calcareous wackestone; mouldic calcite cement in gastropod present in sample	1642	745	1021	417	1585	513	−23.7	2.1	−18.7	4.0	−27.1	2

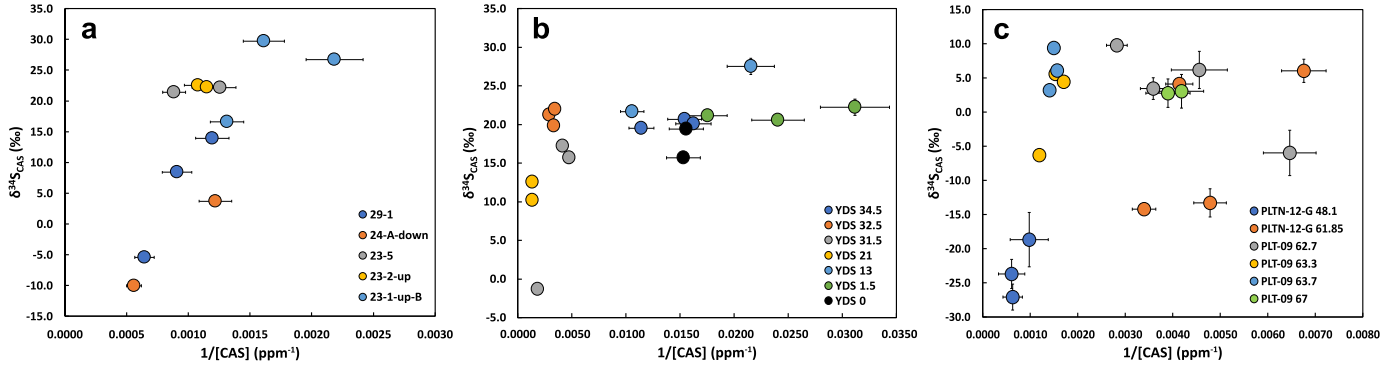

Fig. 2. Plot of $\delta^{34}S_{CAS}$ versus 1/[CAS] (ppm^{-1}) for samples from (A) Meishan, (B) Yudongzi, and (C) Penglaitan. Color denotes hand sample from which each measurement was taken.

Here, $\delta^{34}S_{CAS}$ variations commonly exceed 5‰ and sometimes exceed 10‰. What is the source of this variability?

Plots of $\delta^{34}S_{CAS}$ versus 1/[CAS] suggest an origin of the $\delta^{34}S_{CAS}$ variation (Fig. 2). Meishan data show a strong correlation between $\delta^{34}S_{CAS}$ values and 1/[CAS], with higher [CAS] associated with lower $\delta^{34}S_{CAS}$ values. This trend is muted at Yudongzi and Penglaitan, though the three highest [CAS] samples at each site have anomalously low $\delta^{34}S_{CAS}$ values. These relationships strongly suggest mixing between low [CAS], high $\delta^{34}S$ and high [CAS], low $\delta^{34}S$ phases.

Several possibilities regarding the identity of the high $\delta^{34}S_{CAS}$ phase(s) exist. Evaporite $\delta^{34}S$ data do not exist at sufficiently high temporal resolution to distinguish precise $\delta^{34}S$ variation across the EPME. However, existing evaporite data suggest that seawater SO_4^{2-} $\delta^{34}S$ was approximately 10 ± 1‰ just prior to the PTB (Bernasconi et al., 2017). These data also indicate a rapid, ~20‰ seawater SO_4^{2-} $\delta^{34}S$ increase over ~2 Myr, with up to one-third of the increase occurring prior to the PTB. Conservatively, this suggests that the seawater-derived CAS end member had a $\delta^{34}S_{CAS}$ value between +10 and +22‰. If we treat the upper limit of this range (22‰) as seawater $\delta^{34}S$, our data are reasonably explained by two end member mixing between CAS unaltered from seawater SO_4^{2-} in its $\delta^{34}S$ and a low $\delta^{34}S$, high [CAS] phase. A lower seawater $\delta^{34}S$ would require that most of the data be affected by significant diagenetic incorporation of ^{34}S-enriched SO_4^{2-}. Such incorporation could have occurred via cementation or recrystallization in the presence of pore water SO_4^{2-} affected by microbial SO_4^{2-} reduction (MSR).

Multiple candidates also exist for the high [CAS], low $\delta^{34}S_{CAS}$ end member(s) inferred from our cross plots. Sulfides are typically depleted in ^{34}S due to the normal isotope effect associated with MSR. With the relatively low (< 1000 ppm) [CAS]'s typically observed here, oxidation of reduced sulfur to SO_4^{2-} could easily skew our measurements toward higher [CAS] and lower $\delta^{34}S_{CAS}$ values if this SO_4^{2-} were incorporated into our measured CAS. Alternatively, temporal variation in seawater SO_4^{2-} — i.e., an increase in [SO_4^{2-}] and decrease in $\delta^{34}S$ — could also explain this trend. Carbonate and evaporite mineralogy (Hardie, 1996) and evaporite fluid inclusion data (Lowenstein et al., 2003) argue against low [SO_4^{2-}] at this time and suggest the observed $\delta^{34}S_{CAS}$ changes are too rapid to reflect primary temporal $\delta^{34}S$ variation. Based on these considerations and our within-sample $\delta^{34}S_{CAS}$ heterogeneity, we favor diagenetic incorporation of oxidation-derived SO_4^{2-} as the explanation for the mixing trend in our data. We cannot a priori determine if such oxidation occurred in-situ during deposition or after lithification, but we discuss the possibility of in-situ oxidation below.

5.3. Implications for EPME $\delta^{34}S_{CAS}$

Previous work (e.g. Newton et al., 2004; Schobben et al., 2015) has noted a substantial decrease in SO_4^{2-} $\delta^{34}S$ values associated with the EPME extinction interval (Fig. 3). This decrease is pronounced in CAS $\delta^{34}S$ records (e.g. Kaiho et al., 2001; Schobben et al., 2015) and is present to a lesser degree in evaporite $\delta^{34}S$ data (Bernasconi et al., 2017). Our $\delta^{34}S_{CAS}$ results also include low $\delta^{34}S_{CAS}$ values near and within the extinction interval. Although correlations between our data and previously measured sections are imprecise, the lowest $\delta^{34}S_{CAS}$ values at each site occur before or within the extinction interval; interestingly, the extremely scattered and low $\delta^{34}S_{CAS}$ values measured by Riccardi et al. (2006) and Li et al. (2009) at Shangsi occur in strata deposited up to ~2 Myr prior to the EPME. CAS from the rapidly deposited Penglaitan section (Shen et al., 2019) is also particularly ^{34}S-depleted. The rough temporal correlation of very low $\delta^{34}S_{CAS}$ values across multiple sections is striking. Is there a mechanism to explain such low $\delta^{34}S_{CAS}$ values amid relatively invariant evaporite $\delta^{34}S$ values?

Several studies have suggested oscillating water column redox conditions in shallow EPME sections across the globe. Evidence for redox oscillations includes variation of pyrite framboid size (e.g. Bond and Wignall, 2010), pyrite triple S isotopic compositions (Shen et al., 2011), and total organic carbon abundance and $\delta^{13}C$ changes (Grice et al., 2005). Deep ocean strata in Japan and Canada (e.g. Isozaki, 1997) indicate a decline in deep ocean [O_2] prior to the EPME and a potential for shallow shelf water column redox changes driven by upwelling anoxic deep waters. Oscillations in upwelling and/or primary productivity have commonly been invoked to explain inferred changes in water column redox at Meishan (Xiang et al., 2020; Wei et al., 2020), Penglaitan (Xiang et al., 2021), and other South China localities (Zhang et al., 2020a). Although uranium abundance and isotopic composition data from carbonates have been used to argue for a modern-like fraction of oxygenated seafloor in the Late Permian (Lau et al., 2016), many other data suggest widespread O_2-poor waters in the EPME ocean (e.g. Xiang et al., 2020; Wei et al., 2020; Zhang et al., 2020a).

Changes in sedimentary redox could have had a large effect on $\delta^{34}S_{CAS}$ values; in particular, more extensive penetration of O_2 into sediments and oxidation of reduced S phases could have enabled a large decrease in $\delta^{34}S_{CAS}$ values if some oxidation-derived SO_4^{2-} was created in the region of carbonate recrystallization. To quantitatively test this hypothesis, we created a simple model in which sediments of assigned initial [CAS], $\delta^{34}S_{CAS}$, pyrite abundance, and pyrite $\delta^{34}S$ are subjected to various degrees of pyrite oxidation, with all the oxidized pyrite S being incorporated into the CAS. Although we assumed pyrite to be the material subject to oxidation, other sources of S (e.g. elemental S; Riccardi et al., 2006) could also contribute without invalidating the model. Results from the model for the Meishan samples are shown in Fig. 4A. We found that all

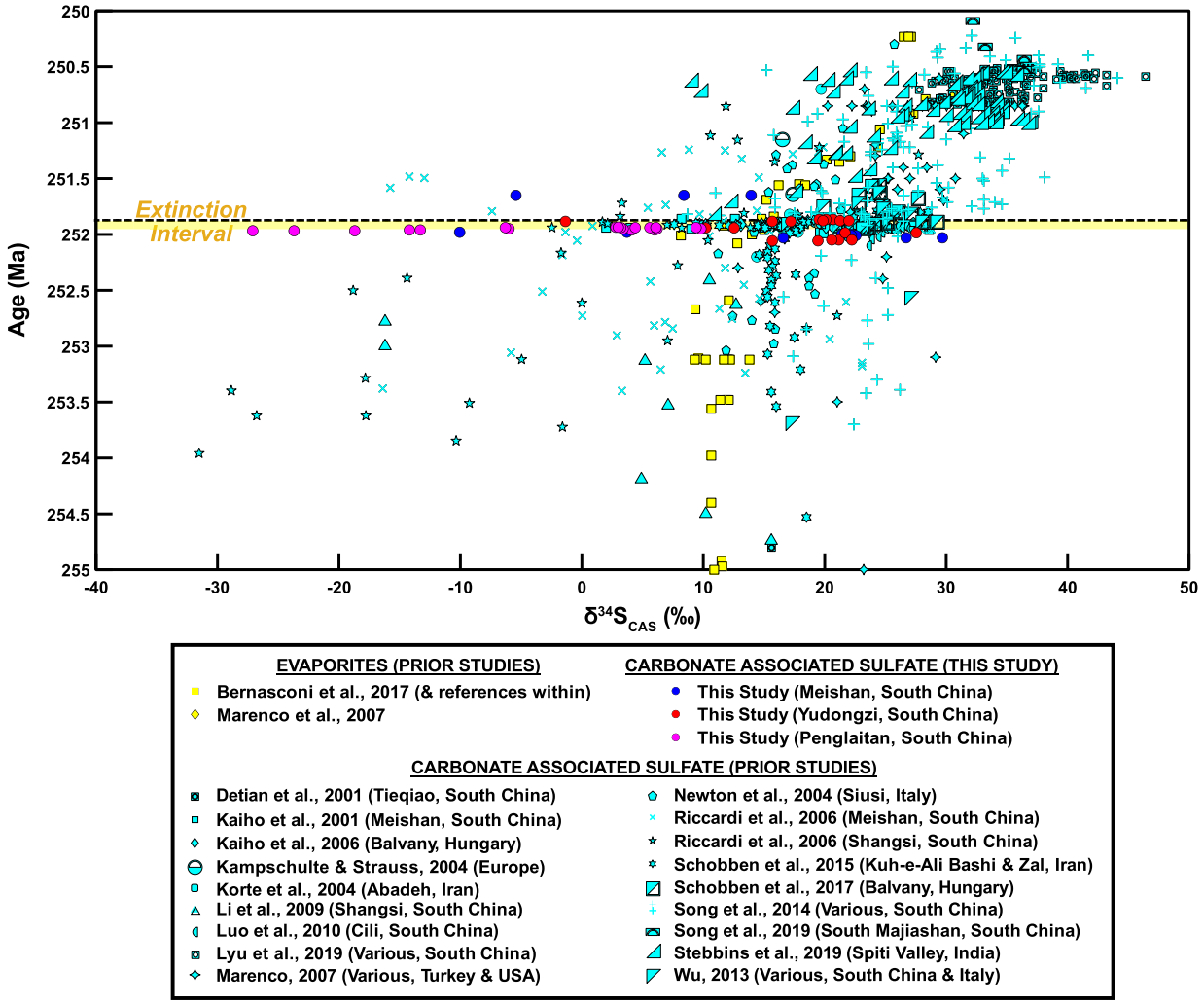

Fig. 3. Plot of $\delta^{34}S$ versus age for our data plus the data of previous studies. All sample ages were updated to the 2012 Geologic Time Scale (Gradstein et al., 2012). Data were correlated based on published stage boundaries and absolute age constraints following previous work (Present et al., 2020). Sedimentation rates were assumed constant between age control points and were extrapolated beyond age control points in rare cases. Each prior study's data from evaporites (yellow) or CAS (cyan) are shown with a unique symbol. This study's data are shown as opaque circles colored based on locality.

our data fall within a [CAS] - $\delta^{34}S_{CAS}$ space in which up to 0.05 wt% S with a $\delta^{34}S$ of $-30‰$ has been oxidized and incorporated as CAS into carbonates with initial [CAS]'s ranging from 400 to 1000 ppm (Fig. 4A). The initial $\delta^{34}S_{CAS}$ value in the model was $+30‰$. Clustering of the data toward the upper left of the plot suggests that most data can be generated via oxidation of far lower amounts of S ($<$ 0.01 wt%). Our model can fit the Yudongzi and Penglaitan data similarly well with slight modifications to the initial conditions (Fig. 4B, C). Notably, the data at Penglaitan fall fully in a compositional space in which the starting $\delta^{34}S_{CAS}$ value was $+10‰$, the approximate $\delta^{34}S$ of end-Permian evaporites (Bernasconi et al., 2017). This may indicate that the pre-oxidation CAS at Penglaitan was unaltered from seawater SO_4^{2-} in its isotopic composition, an interpretation consistent with the site's high sedimentation rate if average rates of carbonate recrystallization were consistent across all sites (Rennie and Turchyn, 2014; Shen et al., 2019). The $+30‰$ initial $\delta^{34}S_{CAS}$ value for Meishan and Yudongzi would consequently reflect pre-oxidative ^{34}S enrichment via MSR, likely the result of early diagenetic carbonate recrystallization under the low to moderate sedimentation rates that characterize these sites (Rennie and Turchyn, 2014; Burgess et al., 2014). The compatibility of these models with our data motivates further study of this scenario.

What processes could be responsible for oscillating sedimentary or water column redox during the EPME, assuming these model trends reflect in-situ oxidation during deposition? Riccardi, Arthur, and Kump (2006) attributed the significant $\delta^{34}S_{CAS}$ variability across the EPME to oscillations in water column redox related to upwelling euxinic waters. Although we agree that the oxidation of solid phase S species seems necessary to generate highly negative $\delta^{34}S_{CAS}$ values (Riccardi et al., 2006), we contend that both the formation and the later oxidation of these species could have occurred entirely within the sediments without necessarily involving water column redox changes. Our estimates for the amount of pyrite oxidation needed to generate the observed $\delta^{34}S_{CAS}$ data via incorporation into CAS are generally similar to or lower than the amount of pyrite S currently preserved in these rocks (e.g. Riccardi et al., 2006). In addition, multiple S isotope data (Shen et al., 2011) suggest that some of the pyrite at Meishan was formed through mixing between H_2S produced from a combination of MSR and S disproportionation and H_2S produced solely from nearly quantitative MSR (i.e., H_2S identical to seawater SO_4^{2-} in its S isotopic composition). Shen et al. (2011) envisioned these variants of pyrite to form in the sediments under differing bottom water redox conditions. However, changes in sedimentation rate, organic matter input, or other sedimentary parameters could have resulted in similar sedimentary redox changes (e.g. Johnson, 2021). We favor a sedimentary locale for the redox changes based on trace metal data suggesting predominantly oxic water column conditions at

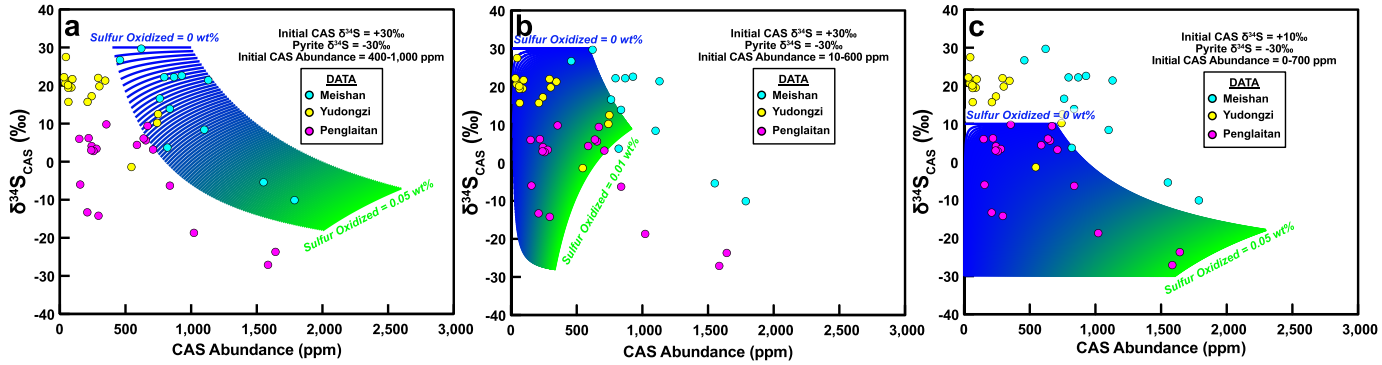

Fig. 4. Plot of final model $\delta^{34}S_{CAS}$ value versus CAS abundance for (A) Meishan, (B) Yudongzi, and (C) Penglaitan. In the models, various amounts of pyrite ($\delta^{34}S = -30‰$) were oxidized and incorporated as CAS. Different lines represent different amounts of oxidized S, with dark blue (top left) denoting no oxidation and lime green (lower right) denoting 0.05 wt% (or 0.01 wt% in panel B) oxidized S. Circles depict data for Meishan (cyan), Yudongzi (yellow), and Penglaitan (magenta).

Penglaitan (Xiang et al., 2021) and trace metal and pyrite framboid size data indicating only sporadic water column euxinia at Meishan (Xiang et al., 2020; Wei et al., 2020). Determining the origin of such synchronous changes in $\delta^{34}S_{CAS}$ variability will be important for understanding changes in biogeochemical cycles across this important time in a mechanistic way.

A sedimentary redox-based origin for the $\delta^{34}S_{CAS}$ heterogeneity within our samples is also consistent with known differences in the depositional environments included within our data compilation (Fig. 3). Meishan, Shangsi, and the Iranian sections analyzed by Schobben et al. (2015) all exhibit facies and age models suggesting very slow sediment accumulation rates ($<$ 3 cm/kyr) immediately prior to the PTB (Riccardi et al., 2006; Burgess et al., 2014; Schobben et al., 2015). In contrast, the Penglaitan and Yudongzi sections analyzed in this study and the Siusi (Newton et al., 2004), Çürük Dağ (Marenco, 2007), and additional South China sections (Luo et al., 2010; Song et al., 2014) analyzed in previous studies all feature shallower water carbonate facies that accumulated at rates several factors to orders of magnitude higher. Notably, most of the shallow water sections except for Penglaitan do not exhibit extremely low $\delta^{34}S_{CAS}$ values near the EPME; the Meishan, Shangsi (Riccardi et al., 2006), and complete Iranian data (Schobben et al., 2015; see their supplementary material) do show lower values before and during the EPME. Prior work in modern marine environments has shown a general correlation of oxygen penetration depth (OPD) in sediments with sedimentation rate; rapidly deposited shelf sediments often feature complete oxygen consumption within ~1 cm of the sediment surface, whereas deeper water sediments bathed in oxic waters on the slope and in the abyss may have OPDs of several to 10s of cm or more (Cai and Sayles, 1996; Hicks et al., 2017). If oscillations in sediment redox were the source of the $\delta^{34}S_{CAS}$ scatter, one would expect sites with slower sediment accumulation rates and deeper oxygen penetration depths (when oxic bottom waters are present) to be disproportionately affected. This largely appears to be the case. Although the Penglaitan sediments exhibit extremely low and scattered $\delta^{34}S_{CAS}$ values despite a high sedimentation rate, it is possible that local conditions permitted especially rapid, productivity-related sediment redox oscillations, particularly given the relatively low ($<$ 0.3 wt%) total organic carbon contents measured in end-Permian strata at the site and an apparent proximity of the site to continental inputs; mixed marine-terrestrial facies are present just tens of meters below the EPME in sediments that postdate 252.359 $\pm$ 0.038 Ma within the section (Shen et al., 2007, 2019).

As a plausibility check, we can estimate the frequency of sedimentary redox oscillations required to oxidize sedimentary sulfides and incorporate them into CAS using a combination of oxygen penetration depth and sediment accumulation rate. For the sake of simplicity, assume that sediment redox oscillations result in

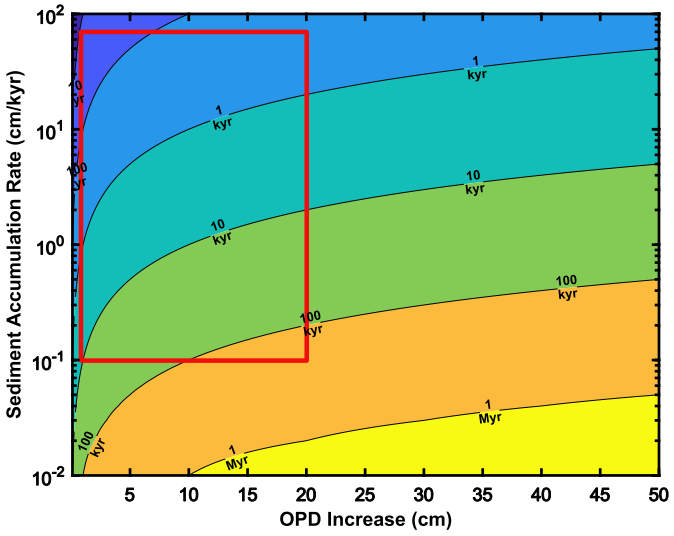

Fig. 5. Contour plot of the maximum allowable period between oxygen penetration depth (OPD) increases for 100% of deposited sediments to be exposed to oxygen as a function of sedimentation rate (vertical axis) and the magnitude of the OPD increase (horizontal axis). Contours and vertical axis increment on a base-10 logarithmic scale. The red box outlines the parameter space pertinent to the Meishan, Yudongzi, and Penglaitan sites analyzed in this study.

the oxygen penetration depth varying from zero to a depth x in the sediment. At a constant sediment accumulation rate w, the amount of time t represented by the sediments newly bathed in oxygen with an OPD increase to depth x is equal to x/w. Assuming that sediment redox oscillations occur at a frequency f, the fraction of the deposited sediment that is affected by the changing sedimentary redox conditions can be calculated by multiplying t by f. We calculated the frequency of sediment redox oscillations required for 100% of the deposited sediment to be affected by a given OPD increase at various sedimentation rates and display the results as a contour plot in Fig. 5. For the range of sedimentation rates (~0.1–70 cm/kyr) documented in this study and an OPD change of up to 20 cm, the frequency at which sediment redox oscillations must occur to expose all deposited sediment to oxic waters can be as infrequent as once per ~100 kyr (for large OPD oscillations and very low sedimentation rates). Even at Penglaitan-like sedimentation rates and small ($<$ 5 cm) OPD changes, sedimentary redox oscillations need only to occur on decadal timescales to periodically expose 100% of the deposited sediment to oxic waters. Sediment compaction, bioturbation, fluctuations in sediment accumulation rate, and other variables undoubtedly add complexity to this scenario. However, the consistency of these timescales with timescales of significant environ-

mental (e.g. primary productivity) variation in the recent geologic past suggests that this mechanism for generating extreme $\delta^{34}S_{CAS}$ heterogeneity and very low $\delta^{34}S_{CAS}$ values may be feasible. These results similarly support previous studies (Schobben et al., 2015) that have qualitatively invoked this mechanism as a possibility. An upwelling-based origin for the redox oscillations remains possible based on these calculations, but perturbations that operate on longer timescales (e.g. orbital forcing of weathering and climate) are also viable. Note that this mechanism *perturbs $\delta^{34}S_{CAS}$ in strata that precede the actual perturbation itself*; i.e., the location of $\delta^{34}S_{CAS}$ scatter in sediments deposited before the EPME does not preclude an EPME origin of the scatter. Nonetheless, extrusive volcanism and apparent environmental stress beginning several hundred kyr prior to the EPME (Grasby et al., 2015; Burgess et al., 2017; Fielding et al., 2019) could also have been a contributing factor in this scenario.

5.4. Framework for assessing the primary nature of $\delta^{34}S_{CAS}$ variability

Prior work has shown that $\delta^{34}S_{CAS}$ measurements can exhibit significant heterogeneity within single hand samples (Present et al., 2015) and among contemporaneous strata in adjacent depositional environments (Present et al., 2019; Richardson et al., 2019). Here, we have confirmed that within-sample $\delta^{34}S_{CAS}$ heterogeneity is present in carbonates deposited across the EPME in South China and may help explain the extreme scatter in the $\delta^{34}S_{CAS}$ values presented in several previous studies (e.g. Riccardi et al., 2006; Li et al., 2009). Such heterogeneity results from the high sensitivity of sulfate $\delta^{34}S$ to early diagenesis (Rennie and Turchyn, 2014); bulk rock $\delta^{34}S_{CAS}$ records must consequently be interpreted to represent ancient seawater sulfate $\delta^{34}S$ values with substantial caution. However, prior work has also suggested that bulk rocks formed under appropriate sedimentary conditions *can* preserve primary or near-primary seawater $\delta^{34}S$ signatures within CAS in some instances (e.g. Rennie and Turchyn, 2014; Schobben et al., 2015; Present et al., 2019). This preservation potential is reflected by Phanerozoic bulk rock $\delta^{34}S_{CAS}$ trends that are indistinguishable from those of other proxies for seawater sulfate $\delta^{34}S$ (Present et al., 2020), albeit with much more short-timescale variability. How should the primary versus diagenetic origin of $\delta^{34}S_{CAS}$ variability in particular temporal records be evaluated given this ambiguity?

Previous work has shown that careful observation of the phases analyzed for $\delta^{34}S_{CAS}$ and consideration of their origin is key to interpreting records (Present et al., 2015, 2019). Retention of primary crystalline textures in biogenic carbonates originally formed in seawater (e.g. Present et al., 2015; Johnson et al., 2020) provides a straightforward indication of $\delta^{34}S_{CAS}$ that likely reflects a primary marine signature; however, early cement phases precipitated under seawater-buffered diagenetic regimes may also be viable marine $\delta^{34}S$ archives (Paris et al., 2014; Roberts et al., 2018b, 2018a; Present et al., 2019). At minimum, textures should be observed in freshly cut and polished samples (ideally thin sections) to understand the nature of the phases that may be incorporated within a single $\delta^{34}S_{CAS}$ measurement. Without such observation, high $\delta^{34}S_{CAS}$ variability should by default be attributed to a secondary origin unless other lines of evidence (e.g. coeval evaporite or barite $\delta^{34}S$ records) suggest an intact primary signal. While the lack of a preserved marine $\delta^{34}S$ signature may initially be disappointing, the EPME data presented here demonstrate that secondary $\delta^{34}S_{CAS}$ signatures can still originate from widespread environmental perturbations and yield valuable information about processes occurring at local to global scales.

Relationships among [CAS], $\delta^{34}S_{CAS}$, redox-active sedimentary phases, and sedimentation rate also provide valuable tools in record interpretation. Our efforts and those of previous studies (e.g. Present et al., 2015) have shown that cross-plots of 1/[CAS] versus $\delta^{34}S_{CAS}$ can indicate a possible mixing origin for $\delta^{34}S_{CAS}$ variability. Within-phase $\delta^{34}S_{CAS}$ heterogeneity (e.g. Kampschulte and Strauss, 2004) and correlation of $\delta^{34}S_{CAS}$ with the concentration and/or isotopic composition of other sedimentary phases (especially organic carbon and iron) may likewise indicate a diagenetic influence even if textures appear to be primary (e.g. Cummins et al., 2014). While observed correlations need not be of secondary origin, the residence times of relevant seawater constituents (e.g. seawater sulfate) suggested by other archives must be carefully considered before invoking a primary origin. Any relationship between $\delta^{34}S_{CAS}$ and sedimentation rate or between $\delta^{34}S_{CAS}$ and the abundance of other sulfur-bearing phases (e.g. pyrite and organic sulfur) should prompt similar skepticism given the influence of sedimentation rate on the $\delta^{34}S$ of authigenic pyrite (Pasquier et al., 2017, 2021) and the potential for contamination of CAS by other phases during laboratory preparation (Marenco et al., 2007; Wotte et al., 2012; Theiling and Coleman, 2015). Such considerations may aid the culling of contaminated data and enable recovery of a more pristine seawater $\delta^{34}S$ signature (e.g. Schobben et al., 2015).

Finally, $\delta^{34}S_{CAS}$ records interpreted to represent primary seawater $\delta^{34}S$ should be consistent with independent lines of evidence such as evaporite fluid inclusion [SO_4^{2-}] estimates (e.g. Lowenstein et al., 2003); barite (e.g. Paytan et al., 1998), evaporite (e.g. Bernasconi et al., 2017), and biogenic CAS (e.g. Kampschulte and Strauss, 2004) $\delta^{34}S$ records; and physical oceanography. An interpretation inconsistent with previous records or involving novel processes (e.g. upwelling of anoxic waters) should be considered only once alteration and contamination have been eliminated as likely explanations. Ideally, novel $\delta^{34}S_{CAS}$ interpretations should be supported by findings from other studies – e.g., the presence of biomarkers associated with photic zone euxinia (Grice et al., 2005). Such leveraging of $\delta^{34}S_{CAS}$ data with other geochemical, geological, and oceanographic constraints will ultimately result in more robust paleoenvironmental reconstructions across time periods beyond the EPME.

6. Summary

Overall, geologic records suggest a dynamic marine system during the EPME. Eruption of the Siberian Traps and associated injection of large amounts of ^{13}C-depleted carbon likely initiated rapid global warming that exerted extreme stress on many marine organisms (e.g. Payne and Clapham, 2012). Development of anoxic deep ocean waters (e.g. Isozaki, 1997) and incursion of these waters into shallow environments (e.g. Bond and Wignall, 2010) may have been a key part of this warming-related stress. Oscillations in sedimentary redox associated with these incursions or with other forcing mechanisms (e.g. variations in primary productivity) can explain the variable $\delta^{34}S_{CAS}$ values and relatively invariant evaporite $\delta^{34}S$ values across the EPME; extremely low seawater [SO_4^{2-}] (e.g. Song et al., 2014) is neither necessary nor likely. The extinction culminated in a massive ocean acidification event (e.g. Hinojosa et al., 2012) coinciding with a large negative carbon isotope excursion (e.g. Payne et al., 2004) across global environments. Persistently low seawater oxygenation may have prevented ecologic recovery until several Myr into the Triassic (e.g. Newton et al., 2004; Lau et al., 2016). Additional careful geochemical work and cautious, informed interpretations of future $\delta^{34}S_{CAS}$ records should allow the interactions between the sulfur cycle and other biogeochemical cycles to be better evaluated during the EPME and beyond.

CRediT authorship contribution statement

Daniel L. Johnson: Conceptualization, Data curation, Formal analysis, Investigation, Methodology, Software, Validation, Visual-

ization, Writing – original draft. **Theodore M. Present:** Conceptualization, Data curation, Investigation, Methodology, Resources, Writing – review & editing. **Menghan Li:** Conceptualization, Methodology. **Yanan Shen:** Conceptualization, Data curation, Funding acquisition, Investigation, Methodology, Project administration, Resources, Supervision, Writing – review & editing. **Jess F. Adkins:** Conceptualization, Funding acquisition, Investigation, Methodology, Project administration, Resources, Supervision, Writing – review & editing.

Declaration of competing interest

The authors declare that they have no known competing financial interests or personal relationships that could have appeared to influence the work reported in this paper.

Acknowledgements

We thank Nathan Dalleska, Jared Marske, and Grace Ames for analytical assistance and Sam Bowring for providing the Penglaitan samples. We also thank Stefano Bernasconi, editor Louis Derry, and an anonymous reviewer for providing thoughtful feedback that allowed us to substantially improve this manuscript. This work was supported by National Science Foundation (NSF) grants OCE-1559215, OCE-1737404, OCE-1450528, and MGG-1834492; NASA prime grant NNN12AA01C; Change Happens Foundation; and Grantham Foundation awards to JFA. DLJ thanks the NSF for GRFP support. ML and YS were supported by National Natural Science Foundation of China (41721002).

Appendix A. Supplementary material

Supplementary material related to this article can be found online at https://doi.org/10.1016/j.epsl.2021.117172.

References

Bernasconi, S.M., Meier, I., Wohlwend, S., Brack, P., Hochuli, P.A., Bläsi, H., Wortmann, U.G., Ramseyer, K., 2017. An evaporite-based high-resolution sulfur isotope record of Late Permian and Triassic seawater sulfate. Geochim. Cosmochim. Acta 204, 331–349. https://doi.org/10.1016/j.gca.2017.01.047.

Bond, D.P.G., Wignall, P.B., 2010. Pyrite framboid study of marine Permian–Triassic boundary sections: a complex anoxic event and its relationship to contemporaneous mass extinction. Geol. Soc. Am. Bull. 122, 1265–1279. https://doi.org/10.1130/B30042.1.

Burgess, S.D., Bowring, S., Shen, S., 2014. High-precision timeline for Earth's most severe extinction. Proc. Natl. Acad. Sci. 111, 3316–3321. https://doi.org/10.1073/pnas.1317692111.

Burgess, S.D., Muirhead, J.D., Bowring, S.A., 2017. Initial pulse of Siberian Traps sills as the trigger of the end-Permian mass extinction. Nat. Commun. 8, 164. https://doi.org/10.1038/s41467-017-00083-9.

Cai, W.-J., Sayles, F.L., 1996. Oxygen penetration depths and fluxes in marine sediments. Mar. Chem. 52, 123–131. https://doi.org/10.1016/0304-4203(95)00081-X.

Cao, C., Love, G.D., Hays, L.E., Wang, W., Shen, S., Summons, R.E., 2009. Biogeochemical evidence for euxinic oceans and ecological disturbance presaging the end-Permian mass extinction event. Earth Planet. Sci. Lett. 281, 188–201. https://doi.org/10.1016/j.epsl.2009.02.012.

Cao, C., Wang, W., Jin, Y., 2002. Carbon isotope excursions across the Permian-Triassic boundary in the Meishan section, Zhejiang Province, China. Chin. Sci. Bull. 47, 1125. https://doi.org/10.1360/02tb9252.

Chen, Z.-Q., et al., 2015. Complete biotic and sedimentary records of the Permian–Triassic transition from Meishan section, South China: ecologically assessing mass extinction and its aftermath. Earth-Sci. Rev. 149, 67–107. https://doi.org/10.1016/j.earscirev.2014.10.005.

Cummins, R.C., Finnegan, S., Fike, D.A., Eiler, J.M., Fischer, W.W., 2014. Carbonate clumped isotope constraints on Silurian ocean temperature and seawater δ18O. Geochim. Cosmochim. Acta 140, 241–258. https://doi.org/10.1016/j.gca.2014.05.024.

Erwin, D.H., 2006. Extinction: How Life on Earth Nearly Ended 250 Million Years Ago. Princeton University Press, Princeton, NJ, US. Extinction: How Life on Earth Nearly Ended 250 Million Years Ago, p. viii, 296.

Fielding, C.R., et al., 2019. Age and pattern of the southern high-latitude continental end-Permian extinction constrained by multiproxy analysis. Nat. Commun. 10, 385. https://doi.org/10.1038/s41467-018-07934-z.

Gradstein, F.M., Ogg, J.G., Schmitz, M., Ogg, G., 2012. The Geologic Time Scale 2012. Elsevier.

Grasby, S.E., Beauchamp, B., Bond, D.P.G., Wignall, P., Talavera, C., Galloway, J.M., Piepjohn, K., Reinhardt, L., Blomeier, D., 2015. Progressive environmental deterioration in northwestern Pangea leading to the latest Permian extinction. Geol. Soc. Am. Bull. 127, 1331–1347. https://doi.org/10.1130/B31197.1.

Grice, K., Cao, C., Love, G.D., Böttcher, M.E., Twitchett, R.J., Grosjean, E., Summons, R.E., Turgeon, S.C., Dunning, W., Jin, Y., 2005. Photic Zone Euxinia During the Permian-Triassic Superanoxic Event. Science 307, 706–709. https://doi.org/10.1126/science.1104323.

Grossman, E.L., Mii, H.-S., Yancey, T.E., 1993. Stable isotopes in Late Pennsylvanian brachiopods from the United States: implications for Carboniferous paleoceanography. Geol. Soc. Am. Bull. 105, 1284–1296.

Grossman, E.L., Zhang, C., Yancey, T.E., 1991. Stable-isotope stratigraphy of brachiopods from Pennsylvanian shales in Texas. Geol. Soc. Am. Bull. 103, 953–965.

Hardie, L.A., 1996. Secular variation in seawater chemistry: an explanation for the coupled secular variation in the mineralogies of marine limestones and potash evaporites over the past 600 m.y. Geology 24, 279–283. https://doi.org/10.1130/0091-7613(1996)024<0279:SVISCA>2.3.CO;2.

Hicks, N., et al., 2017. Oxygen dynamics in shelf seas sediments incorporating seasonal variability. Biogeochemistry 135, 35–47. https://doi.org/10.1007/s10533-017-0326-9.

Hinojosa, J.L., Brown, S.T., Chen, J., DePaolo, D.J., Paytan, A., Shen, S., Payne, J.L., 2012. Evidence for end-Permian ocean acidification from calcium isotopes in biogenic apatite. Geology 40, 743–746. https://doi.org/10.1130/G33048.1.

Hongfu, Y., Kexin, Z., Jinnan, T., Zunyi, Y., Shunbao, W., 2001. The global stratotype section and point (GSSP) of the Permian-Triassic boundary. Episodes 24, 102–114.

Isozaki, Y., 1997. Permo-Triassic Boundary Superanoxia and Stratified Superocean: Records from Lost Deep Sea. Science 276, 235–238. https://doi.org/10.1126/science.276.5310.235.

Jin, Y., Shen, S., Henderson, C.M., Wang, X., Wang, W., Wang, Y., Cao, C., Shang, Q., 2006. The Global Stratotype Section and Point (GSSP) for the boundary between the Capitanian and Wuchiapingian stage (Permian).

Johnson, D.L., 2021. Sulfur Isotopic Insights into the Modern and Ancient Marine Sulfur Cycles. Ph.D. Thesis California Institute of Technology. https://doi.org/10.7907/vc71-ht05.

Johnson, D.L., Grossman, E.L., Webb, S.M., Adkins, J.F., 2020. Brachiopod δ34SCAS microanalyses indicate a dynamic, climate-influenced Permo-Carboniferous sulfur cycle. Earth Planet. Sci. Lett. 546, 116428. https://doi.org/10.1016/j.epsl.2020.116428.

Kaiho, K., Kajiwara, Y., Nakano, T., Miura, Y., Kawahata, H., Tazaki, K., Ueshima, M., Chen, Z., Shi, G.R., 2001. End-Permian catastrophe by a bolide impact: evidence of a gigantic release of sulfur from the mantle. Geology 29, 815–818. https://doi.org/10.1130/0091-7613(2001)029<0815:EPCBAB>2.0.CO;2.

Kampschulte, A., Strauss, H., 2004. The sulfur isotopic evolution of Phanerozoic seawater based on the analysis of structurally substituted sulfate in carbonates. Chem. Geol. 204, 255–286. https://doi.org/10.1016/j.chemgeo.2003.11.013.

Kershaw, S., et al., 2012. Microbialites and global environmental change across the Permian–Triassic boundary: a synthesis. Geobiology 10, 25–47. https://doi.org/10.1111/j.1472-4669.2011.00302.x.

Knoll, A.H., Bambach, R.K., Payne, J.L., Pruss, S., Fischer, W.W., 2007. Paleophysiology and end-Permian mass extinction. Earth Planet. Sci. Lett. 256, 295–313. https://doi.org/10.1016/j.epsl.2007.02.018.

Korte, C., Kozur, H.W., Joachimski, M.M., Strauss, H., Veizer, J., Schwark, L., 2004. Carbon, sulfur, oxygen and strontium isotope records, organic geochemistry and biostratigraphy across the Permian/Triassic boundary in Abadeh, Iran. Int. J. Earth Sci. 93, 565–581. https://doi.org/10.1007/s00531-004-0406-7.

Lau, K.V., Maher, K., Altiner, D., Kelley, B.M., Kump, L.R., Lehrmann, D.J., Silva-Tamayo, J.C., Weaver, K.L., Yu, M., Payne, J.L., 2016. Marine anoxia and delayed Earth system recovery after the end-Permian extinction. Proc. Natl. Acad. Sci. 113, 2360–2365. https://doi.org/10.1073/pnas.1515080113.

Li, P., Huang, J., Chen, M., Bai, X., 2009. Coincident negative shifts in sulfur and carbon isotope compositions prior to the end-Permian mass extinction at Shangsi Section of Guangyuan, South China. Front. Earth Sci. China 3, 51. https://doi.org/10.1007/s11707-009-0018-4.

Lowenstein, T.K., Hardie, L.A., Timofeeff, M.N., Demicco, R.V., 2003. Secular variation in seawater chemistry and the origin of calcium chloride basinal brines. Geology 31, 857–860. https://doi.org/10.1130/g19728r.1.

Luo, G., Kump, L.R., Wang, Y., Tong, J., Arthur, M.A., Yang, H., Huang, J., Yin, H., Xie, S., 2010. Isotopic evidence for an anomalously low oceanic sulfate concentration following end-Permian mass extinction. Earth Planet. Sci. Lett. 300, 101–111. https://doi.org/10.1016/j.epsl.2010.09.041.

Marenco, P.J., 2007. Sulfur Isotope Geochemistry and the End Permian Mass Extinction. University of Southern California.

Marenco, P.J., Corsetti, F.A., Hammond, D.E., Kaufman, A.J., Bottjer, D.J., 2007. Oxidation of pyrite during extraction of carbonate associated sulfate. Chem. Geol. 247, 124–132. https://doi.org/10.1016/j.chemgeo.2007.10.006.

Marenco, P.J., Corsetti, F.A., Kaufman, A.J., Bottjer, D.J., 2008. Environmental and diagenetic variations in carbonate associated sulfate: an investigation of CAS in the Lower Triassic of the western USA. Geochim. Cosmochim. Acta 72, 1570–1582. https://doi.org/10.1016/j.gca.2007.10.033.

Newton, R.J., Pevitt, E.L., Wignall, P.B., Bottrell, S.H., 2004. Large shifts in the isotopic composition of seawater sulphate across the Permo–Triassic boundary in northern Italy. Earth Planet. Sci. Lett. 218, 331–345. https://doi.org/10.1016/S0012-821X(03)00676-9.

Paris, G., Adkins, J.F., Sessions, A.L., Webb, S.M., Fischer, W.W., 2014. Neoarchean carbonate–associated sulfate records positive Δ33S anomalies. Science 346, 739–741. https://doi.org/10.1126/science.1258211.

Paris, G., Sessions, A.L., Subhas, A.V., Adkins, J.F., 2013. MC-ICP-MS measurement of δ34S and Δ33S in small amounts of dissolved sulfate. Chem. Geol. 345, 50–61. https://doi.org/10.1016/j.chemgeo.2013.02.022.

Pasquier, V., Bryant, R.N., Fike, D.A., Halevy, I., 2021. Strong local, not global, controls on marine pyrite sulfur isotopes. Sci. Adv. 7, eabb7403. https://doi.org/10.1126/sciadv.abb7403.

Pasquier, V., Sansjofre, P., Rabineau, M., Revillon, S., Houghton, J., Fike, D.A., 2017. Pyrite sulfur isotopes reveal glacial-interglacial environmental changes. Proc. Natl. Acad. Sci. 114, 5941–5945. https://doi.org/10.1073/pnas.1618245114.

Payne, J.L., Clapham, M.E., 2012. End-Permian Mass Extinction in the Oceans: An Ancient Analog for the Twenty-First Century? https://doi.org/10.1146/annurev-earth-042711-105329.

Payne, J.L., Lehrmann, D.J., Wei, J., Orchard, M.J., Schrag, D.P., Knoll, A.H., 2004. Large perturbations of the carbon cycle during recovery from the End-Permian extinction. Science 305, 506–509. https://doi.org/10.1126/science.1097023.

Paytan, A., Kastner, M., Campbell, D., Thiemens, M.H., 1998. Sulfur isotopic composition of Cenozoic seawater sulfate. Science 282, 1459–1462. https://doi.org/10.1126/science.282.5393.1459.

Present, T.M., Adkins, J.F., Fischer, W.W., 2020. Variability in sulfur isotope records of Phanerozoic seawater sulfate. Geophys. Res. Lett. 47, e2020GL088766. https://doi.org/10.1029/2020GL088766.

Present, T.M., Gutierrez, M., Paris, G., Kerans, C., Grotzinger, J.P., Adkins, J.F., 2019. Diagenetic controls on the isotopic composition of carbonate-associated sulphate in the Permian Capitan Reef Complex, West Texas. Sedimentology 66, 2605–2626. https://doi.org/10.1111/sed.12615.

Present, T.M., Paris, G., Burke, A., Fischer, W.W., Adkins, J.F., 2015. Large Carbonate Associated Sulfate isotopic variability between brachiopods, micrite, and other sedimentary components in Late Ordovician strata. Earth Planet. Sci. Lett. 432, 187–198. https://doi.org/10.1016/j.epsl.2015.10.005.

Rennie, V.C.F., Turchyn, A.V., 2014. The preservation of d34S and d18O in carbonate-associated sulfate during marine diagenesis: a 25 Myr test case using marine sediments. Earth Planet. Sci. Lett. 395, 13–23. https://doi.org/10.1016/j.epsl.2014.03.025.

Riccardi, A.L., Arthur, M.A., Kump, L.R., 2006. Sulfur isotopic evidence for chemocline upward excursions during the end-Permian mass extinction. Geochim. Cosmochim. Acta 70, 5740–5752. https://doi.org/10.1016/j.gca.2006.08.005.

Richardson, J.A., Keating, C., Lepland, A., Hints, O., Bradley, A.S., Fike, D.A., 2019. Silurian records of carbon and sulfur cycling from Estonia: the importance of depositional environment on isotopic trends. Earth Planet. Sci. Lett. 512, 71–82. https://doi.org/10.1016/j.epsl.2019.01.055.

Roberts, J., Kaczmarek, K., Langer, G., Skinner, L.C., Bijma, J., Bradbury, H., Turchyn, A.V., Lamy, F., Misra, S., 2018a. Lithium isotopic composition of benthic foraminifera: a new proxy for paleo-pH reconstruction. Geochim. Cosmochim. Acta 326, 336–350. https://doi.org/10.1016/j.gca.2018.02.038.

Roberts, J., Turchyn, A.V., Wignall, P.B., Newton, R.J., Vane, C.H., 2018b. Disentangling Diagenesis From the Rock Record: An Example From the Permo-Triassic Wordie Creek Formation, East Greenland. Geochem. Geophys. Geosyst. 19, 99–113. https://doi.org/10.1002/2017GC007259.

Schobben, M., Stebbins, A., Ghaderi, A., Strauss, H., Korn, D., Korte, C., 2015. Flourishing ocean drives the end-Permian marine mass extinction. Proc. Natl. Acad. Sci. 112, 10298–10303. https://doi.org/10.1073/pnas.1503755112.

Schoepfer, S.D., Henderson, C.M., Garrison, G.H., Foriel, J., Ward, P.D., Selby, D., Hower, J.C., Algeo, T.J., Shen, Y., 2013. Termination of a continent-margin upwelling system at the Permian–Triassic boundary (Opal Creek, Alberta, Canada. Glob. Planet. Change 105, 21–35. https://doi.org/10.1016/j.gloplacha.2012.07.005.

Scotese, C.R., 2014. Atlas of Permo-Carboniferous Paleogeographic Maps (Mollweide Projection), Maps 53–64, Volumes 4, The Late Paleozoic, PALEOMAP Atlas for ArcGIS. PALEOMAP Project, Evanston, IL..

Sepkoski, J.J., 1981. A factor analytic description of the Phanerozoic marine fossil record. Paleobiology 7, 36–53. https://doi.org/10.1017/S0094837300003778.

Shen, S.-Z., et al., 2019. A sudden end-Permian mass extinction in South China. Geol. Soc. Am. Bull. 131, 205–223. https://doi.org/10.1130/B31909.1.

Shen, Y., Farquhar, J., Zhang, H., Masterson, A., Zhang, T., Wing, B.A., 2011. Multiple S-isotopic evidence for episodic shoaling of anoxic water during Late Permian mass extinction. Nat. Commun. 2, 210. https://doi.org/10.1038/ncomms1217.

Shen, S.-Z., Wang, Y., Henderson, C.M., Cao, C.-Q., Wang, W., 2007. Biostratigraphy and lithofacies of the Permian System in the Laibin–Heshan area of Guangxi, South China. Palaeoworld 16, 120–139. https://doi.org/10.1016/j.palwor.2007.05.005.

Song, H., et al., 2014. Early Triassic seawater sulfate drawdown. Geochim. Cosmochim. Acta 128, 95–113. https://doi.org/10.1016/j.gca.2013.12.009.

Svensen, H., Planke, S., Polozov, A.G., Schmidbauer, N., Corfu, F., Podladchikov, Y.Y., Jamtveit, B., 2009. Siberian gas venting and the end-Permian environmental crisis. Earth Planet. Sci. Lett. 277, 490–500. https://doi.org/10.1016/j.epsl.2008.11.015.

Tang, H., et al., 2017. Permian–Triassic boundary microbialites (PTBMs) in southwest China: implications for paleoenvironment reconstruction. Facies 63, 2. https://doi.org/10.1007/s10347-016-0482-8.

Theiling, B.P., Coleman, M., 2015. Refining the extraction methodology of carbonate associated sulfate: evidence from synthetic and natural carbonate samples. Chem. Geol. 411, 36–48. https://doi.org/10.1016/j.chemgeo.2015.06.018.

Veizer, J., et al., 1999. 87Sr/86Sr, δ13C and δ18O evolution of Phanerozoic seawater. Chem. Geol. 161, 59–88. https://doi.org/10.1016/S0009-2541(99)00081-9.

Wei, H., Zhang, X., Qiu, Z., 2020. Millennial-scale ocean redox and δ13C changes across the Permian–Triassic transition at Meishan and implications for the biocrisis. Int. J. Earth Sci. 109, 1753–1766. https://doi.org/10.1007/s00531-020-01869-x.

Wotte, T., Shields-Zhou, G.A., Strauss, H., 2012. Carbonate-associated sulfate: experimental comparisons of common extraction methods and recommendations toward a standard analytical protocol. Chem. Geol. 326-327, 132–144. https://doi.org/10.1016/j.chemgeo.2012.07.020.

Xiang, L., Schoepfer, S.D., Yuan, D.-X., Zheng, Q.-F., Zhang, H., 2021. Oceanic redox evolution across the end-Permian mass extinction at Penglaitan section, South China. Palaeoworld. https://doi.org/10.1016/j.palwor.2021.02.003.

Xiang, L., Zhang, H., Schoepfer, S.D., Cao, C., Zheng, Q., Yuan, D., Cai, Y., Shen, S., 2020. Oceanic redox evolution around the end-Permian mass extinction at Meishan, South China. Palaeogeogr. Palaeoclimatol. Palaeoecol. 544, 109626. https://doi.org/10.1016/j.palaeo.2020.109626.

Zhang, L.-J., Zhang, X., Buatois, L.A., Mángano, M.G., Shi, G.R., Gong, Y.-M., Qi, Y.-A., 2020a. Periodic fluctuations of marine oxygen content during the latest Permian. Glob. Planet. Change 195, 103326. https://doi.org/10.1016/j.gloplacha.2020.103326.

Zhang, X.-Y., Zheng, Q.-F., Li, Y., Yang, H.-Q., Zhang, H., Wang, W.-Q., Shen, S.-Z., 2020b. Polybessurus-like fossils as key contributors to Permian–Triassic boundary microbialites in South China. Palaeogeogr. Palaeoclimatol. Palaeoecol. 552, 109770. https://doi.org/10.1016/j.palaeo.2020.109770.

Zheng, Q., Cao, C., Zhang, M., 2013. Sedimentary features of the Permian-Triassic boundary sequence of the Meishan section in Changxing County, Zhejiang Province. Sci. China Earth Sci. 56, 956–969. https://doi.org/10.1007/s11430-013-4602-9.

References in Fig. 3

Detian, Y., Liqin, Z., Zhen, Q., 2013. Carbon and sulfur isotopic fluctuations associated with the end-Guadalupian mass extinction in South China. Gondwana Res. 24, 1276–1282. https://doi.org/10.1016/j.gr.2013.02.008.

Kaiho, K., Kajiwara, Y., Chen, Z.-Q., Gorjan, P., 2006. A sulfur isotope event at the end of the Permian. Chem. Geol. 235, 33–47. https://doi.org/10.1016/j.chemgeo.2006.06.001.

Lyu, Z., Zhang, L., Algeo, T.J., Zhao, L., Chen, Z.-Q., Li, C., Ma, B., Ye, F., 2019. Global-ocean circulation changes during the Smithian–Spathian transition inferred from carbon-sulfur cycle records. Earth-Sci. Rev. 195, 114–132. https://doi.org/10.1016/j.earscirev.2019.01.010.

Schobben, M., Stebbins, A., Algeo, T.J., Strauss, H., Leda, L., Haas, J., Struck, U., Korn, D., Korte, C., 2017. Volatile earliest Triassic sulfur cycle: a consequence of persistent low seawater sulfate concentrations and a high sulfur cycle turnover rate? Palaeogeogr. Palaeoclimatol. Palaeoecol. 486, 74–85. https://doi.org/10.1016/j.palaeo.2017.02.025.

Song, H., Du, Y., Algeo, T.J., Tong, J., Owens, J.D., Song, H., Tian, L., Qiu, H., Zhu, Y., Lyons, T.W., 2019. Cooling-driven oceanic anoxia across the Smithian/Spathian boundary (mid-Early Triassic). Earth-Sci. Rev. 195, 133–146. https://doi.org/10.1016/j.earscirev.2019.01.009.

Stebbins, A., Algeo, T.J., Olsen, C., Sano, H., Rowe, H., Hannigan, R., 2019. Sulfur-isotope evidence for recovery of seawater sulfate concentrations from a PTB minimum by the Smithian-Spathian transition. Earth-Sci. Rev. 195, 83–95. https://doi.org/10.1016/j.earscirev.2018.08.010.

Wu, N., 2013. Sulfur isotopic evolution of Phanerozoic and Ediacaran seawater sulfate.